AGU PUBLICATIONS

Space Weather

RESEARCH ARTICLE
10.1002/2015SW001286

The utility of polarized heliospheric imaging for space weather monitoring

C. E. DeForest[1], T. A. Howard[1], D. F. Webb[2], and J. A. Davies[3]

[1]Department of Space Studies, Southwest Research Institute, Boulder, Colorado, USA, [2]Institute of Space Research, Boston College, Chestnut Hill, Massachusetts, USA, [3]STFC-RAL Space, Didcot, UK

Key Points:
- Polarized heliospheric imaging is a necessary next step for improved space weather prediction
- Polarized heliospheric imaging is feasible with current technology
- Polarization is a useful augmentation to current instruments, either on or off the Earth-Sun line

Correspondence to:
C. E. DeForest,
deforest@boulder.swri.edu

Citation:
DeForest, C. E., T. A. Howard, D. F. Webb, and J. A. Davies (2016), The utility of polarized heliospheric imaging for space weather monitoring, *Space Weather*, *14*, 32–49, doi:10.1002/2015SW001286.

Received 14 AUG 2015
Accepted 10 DEC 2015
Accepted article online 15 DEC 2015
Published online 30 JAN 2016

Abstract A polarizing heliospheric imager is a critical next generation tool for space weather monitoring and prediction. Heliospheric imagers can track coronal mass ejections (CMEs) as they cross the solar system, using sunlight scattered by electrons in the CME. This tracking has been demonstrated to improve the forecasting of impact probability and arrival time for Earth-directed CMEs. Polarized imaging allows locating CMEs in three dimensions from a single vantage point. Recent advances in heliospheric imaging have demonstrated that a polarized imager is feasible with current component technology. Developing this technology to a high technology readiness level is critical for space weather relevant imaging from either a near-Earth or deep-space mission. In this primarily technical review, we develop preliminary hardware requirements for a space weather polarizing heliospheric imager system and outline possible ways to flight qualify and ultimately deploy the technology operationally on upcoming specific missions. We consider deployment as an instrument on NOAA's *Deep Space Climate Observatory* follow-on near the Sun-Earth L1 Lagrange point, as a stand-alone constellation of smallsats in low Earth orbit, or as an instrument located at the Sun-Earth L5 Lagrange point. The critical first step is the demonstration of the technology, in either a science or prototype operational mission context.

1. Introduction

There is a strong need for tracking technology to improve space weather prediction. Tracking and visually identifying coronal mass ejections (CMEs) and corotating interaction regions (CIRs) are critical to predicting impact probability, arrival time, and expected ram pressure—three key aspects of successful geomagnetic storm prediction. Current CME prediction techniques used by the U.S. government rely primarily on coronagraphs (e.g., *SOHO*/Large Angle and Spectrometric Coronagraph (LASCO), *STEREO/Coronagraph (COR)*) and modeling [e.g., *Odstrcil and Pizzo*, 1999; *Lee et al.*, 2013] to identify CMEs and estimate the parameters describing their arrival at the Earth [e.g., *Odstrcil et al.*, 2005; *Taktakishvili et al.*, 2009], although other techniques are used scientifically, e.g., interplanetary scintillation [e.g., *Tokumaru*, 2013; *Jackson et al.*, 2013]. Similarly, prediction of CIR arrival at Earth currently relies almost exclusively on solar wind modeling from magnetic structures measured on the surface of the Sun (e.g. the Wang-Sheeley-Arge+Enlil model, [*Broiles et al.*, 2013]). With the advent of wide-angle heliospheric imaging, it became possible to track CMEs and CIRs over wide fields of view, following them continuously on their course from Sun to Earth. Two missions (*Coriolis* and STEREO) have demonstrated the scientific and predictive utility of this continuous tracking. Recent improvements in photometric analysis of heliospheric images suggest that it is now feasible to use a *polarizing* instrument to locate, identify, and track CMEs and CIRs in three dimensions, potentially greatly improving predictive power over what can be achieved with unpolarized instruments now.

A heliospheric imager uses the same physics as a coronagraph, that is, it observes broadband visible light that has been Thomson-scattered off free electrons in the plasma observed by the imager. The difference between the two types of instrument is that a heliospheric imager operates over a very wide field of view (FOV), observing primarily solar wind features in interplanetary space, while a coronagraph typically observes plasma in the solar corona. Together with a coronagraph, a heliospheric imager can track CMEs and their entrained magnetic structures continuously from Sun to Earth [*Howard and DeForest*, 2012b], improving both arrival time and geoeffectiveness prediction.

NASA's scientific STEREO mission is a pathfinder for space weather prediction. Launched in late 2006, it has both coronagraphs and *nonpolarizing* heliospheric imagers [*Howard et al.*, 2008]. Results from STEREO

have shown that unpolarized CME tracking by both coronagraphs and heliospheric imagers improves arrival time prediction by a factor near two, compared to predictions from coronagraph data and modeling alone [*Howard and Tappin*, 2010; *Davis et al.*, 2011; *Webb et al.*, 2013]. Further, it improves understanding of event ram pressure and entrained mass [e.g., *DeForest et al.*, 2013b]. Tracking geoeffective CMEs requires either the imaging of each CME from at least one vantage point away from the Sun-Earth line (for stereoscopic analysis) [e.g., *de Koning et al.*, 2009] or imaging and measuring the three-dimensional location of each CME from a vantage point on the Sun-Earth line.

The polarization properties of Thomson scattering permit more accurate localization of solar wind features in three dimensions. This technique has been used in the corona [e.g., *Poland and Munro*, 1976; *Crifo et al.*, 1983; *Moran et al.*, 2010; *de Koning and Pizzo*, 2011] but is subject to a front/back ambiguity due to the symmetry and restricted geometry of the coronagraph system. This symmetry is broken and the ambiguity eliminated by the wide-field geometry of the heliospheric imaging system [*DeForest et al.*, 2013a]. This would enable the tracking of CMEs and other features in three dimensions from the Sun to the Earth (and beyond), using a relatively low-cost, near-Earth mission. Tracking CMEs with a polarizing heliospheric imager located near the Sun-Earth line could reduce arrival time uncertainty compared to what is possible with current unpolarized imaging, even unpolarized imaging from multiple viewpoints [e.g., *Webb et al.*, 2013].

We are now in the second decade of the heliospheric imaging era, and with two of the three current heliospheric imagers—the Solar Mass Ejection Imager (SMEI) [*Eyles et al.*, 2003] on Coriolis in high LEO and the Heliospheric Imager (HI) on the Solar Terrestrial Relations Observatory (STEREO) "B" spacecraft [*Howard et al.*, 2008]—either deactivated or out of commission, there is currently only one functioning heliospheric imager available (the HI instrument on board STEREO A). It is therefore timely to consider the next steps in future heliospheric imager design. This paper focuses upon the application of heliospheric imagers to space weather prediction and describes specific concepts for future missions; it is not a full review of the extensive scientific work that has been done. For such reviews, the reader may consider the works of *Harrison et al.* [2009, 2012], *Howard* [2011, 2015], and *Rollett et al.* [2014]. The following sections give an overview of the current state of heliospheric imaging (section 2), describe the polarization properties of Thomson-scattered light (section 3), list high-level requirements for an operational imager (section 4), summarize several development pathways to exploit polarized heliospheric imaging (section 5), and recommend a path to space weather prediction using a polarized heliospheric imager in LEO, near L1, or near L5.

2. The State of the Art of Heliospheric Imaging

The main technical challenge of heliospheric imaging is separating the solar wind signal from the far brighter background sources that are present in wide-field visible light images. Both a photometrically precise instrument and an effective signal separation postprocess are needed. The solar wind features of interest (CMEs and CIRs) are wide, distributed objects, and their brightness is thus best described via radiance: power delivered per unit area of aperture, per unit solid angle of sky. Because solar wind features scatter sunlight via Thomson scattering, the natural radiance unit is the mean solar photospheric brightness, $B_\odot$. The numeric value of $B_\odot$ is 2.3×10^7 W m^{-2} sr^{-1}, where *sr* refers to the steradian unit of solid angle. CMEs observed 45° from the Sun typically have a radiance of $\sim 10^{-15} B_\odot$. However, the *F* corona (zodiacal light) and starfield have typical radiances of a few $\times 10^{-14} B_\odot$, 45° from the Sun, so identifying and tracking a CME requires relative photometry and signal separation with a precision of 10^{-2}, and the photometric analysis of CMEs requires precision of 10^{-3}–10^{-4}.

Heliospheric imaging was demonstrated as a feasible detection technology by *Jackson and Leinert* [1985] using data from the Helios photometers. The first dedicated heliospheric imager, Coriolis/SMEI [*Eyles et al.*, 2003], used a similar scanning-detector format in an 850 km altitude, circular polar orbit (at the bottom of the Van Allen radiation belts), with quasi-1-D detectors rather than the three discrete 0-D (single-pixel) photometers of Helios. The SMEI team ultimately was successful at tracking and reconstructing CMEs and CIRs using tools such as the TH model [*Tappin and Howard*, 2009b] and image-constrained kinematic tomography [e.g., *Jackson et al.*, 2006, 2008]. Subsequent wide-field imaging technology includes the "crystal ball" trumpet design developed by *Buffington* [1998] and *Buffington et al.* [1998], which yields a full hemispheric image with excellent external stray light properties, at the cost of incurring a nonuniform PSF and variable polarization properties. More recently, the STEREO/HI instruments [*Eyles et al.*, 2009] introduced the concept of deep baffling and a conventional 2-D image plane detector. For the first years of the STEREO mission, the

main use of the heliospheric imagers was to track the fronts of bright solar wind structures [e.g., *Rouillard et al.*, 2008; *Davies et al.*, 2009; *Wood et al.*, 2012]. This usage has yielded major scientific progress but continued progress in remote sensing requires more sophisticated analysis. *DeForest et al.* [2011] have demonstrated that with improved in-depth data processing, results from the HI instruments can be pushed beyond the ability to simply observe and track CMEs. Work with this new data pipeline includes the measurement of small faint features entrained in the solar wind [e.g., *Howard et al.*, 2012; *Howard and DeForest*, 2015] and CME substructure [e.g., *DeForest et al.*, 2013b; *Howard and DeForest*, 2014]. Noise analysis work by *DeForest and Howard* [2015] shows that instrument characterization and data postprocessing are as important as the instrument technology itself. Refracting optics such as the STEREO/HI instruments are sufficient to image and track CMEs and other space-weather-relevant features through the inner heliosphere, provided that the instrument can be sufficiently well characterized for high-precision relative photometry [e.g., *Bewsher et al.*, 2010; *Tappin et al.*, 2015, 2010] and also that potential in-flight changes of this characterization can be tracked by in-flight calibrations [e.g., *Bewsher et al.*, 2012, 2010].

2.1. Direct Imaging: Demonstrated With STEREO/HI

STEREO/HI demonstrated that full image-plane optics are a feasible means to wide-field unpolarized heliospheric imaging [*Eyles et al.*, 2009]. The STEREO/HI-2 cameras are small (22 mm focal length, 7 mm (f/3.1) aperture) and enclosed in an ~80 cm baffle. Stray light is estimated to be 100× below the *F* corona background [*Eyles et al.*, 2009; *Bewsher et al.*, 2010], and individual data frames are integrated for 5000 s for a cadence of 2 h. The photon noise level is estimated to be $\sim 5 \times 10^{-18} B_\odot$ in each square degree of sky in the *F* corona, 40° from the Sun [*DeForest and Howard*, 2015]. These camera characteristics form a useful baseline that we can scale for the design of future instruments. In this section we describe how some of the problems associated with background subtraction are overcome and explore pathways for future heliospheric imagers.

2.2. Background Subtraction From Deep Space: Solved

DeForest et al. [2011] describe an improved background subtraction method for the STEREO/HI-2 images. Their method exploits differences in form and temporal variation between the background light sources in the HI-2 image stream and the data of interest. It relies on careful photometric calibration of the detectors in the STEREO/HIs [*Bewsher et al.*, 2010, 2012; *Tappin et al.*, 2015]. The resulting photometric data have been used to estimate the masses of CMEs [*DeForest et al.*, 2013b] and other dense solar wind structures [*DeForest et al.*, 2012; *Howard and DeForest*, 2015]. Unpolarized "feature-excess brightness" of bright solar wind features can now be determined with a signal-to-noise ratio of order 30, well away from the Sun.

Prior to the release of processed photometric images, much progress was made using running difference imagery. Such works include *Harrison et al.* [2008], *Davis et al.* [2009], *Wood and Howard* [2009], *Wood et al.* [2011], *Lugaz* [2010], *Möstl et al.* [2010], *Sheeley and Rouillard* [2010], and *Rouillard et al.* [2011]. By around 2010, workers began searching for the means by which they could "drill" farther into the HI data sets, particularly for HI-2, where measurements were mostly limited to geometric and kinematic analysis. Figure 1 demonstrates the relative improvement in feature-excess photometry from prior pipelines for STEREO data. It marks a substantial leap from qualitative imaging, which reveals the location of the fronts of CMEs and other features, to quantitative imaging, which reveals location, photometric brightness, and details about the substructure of the feature of interest. This enables new types of analysis, including mass estimation and polarization analysis (see sections 3.2 and 3.4). The dominant remaining noise source after our postprocessing consists of background residuals due to as yet uncorrected nonlinear effects in the STEREO/HI detector calibration. The final noise level in each square degree is a few $\times 10^{-17} B_\odot$, which is considerably larger than the photon noise alone [*DeForest and Howard*, 2015].

2.3. Background Subtraction From LEO: Feasible

Heliospheric imaging can be accomplished either from deep space (e.g., at L1 or L5) or, more affordably, from low Earth orbit (LEO). LEO has higher visible light background than deep space due to three effects: ram airglow from the host orbital spacecraft, high altitude aurora, and the nearby moon.

Ram Airglow. Ram airglow was measured directly from *Skylab* (235 km altitude) by *Weinberg et al.* [1975] and *Sparrow et al.* [1977]. They found it to be of order $2 \times 10^{-14} B_\odot$, which is about an order of magnitude fainter than the *F* corona (zodiacal light) at ~30° from the Sun. The UV airglow, dominated by ram effects, was measured from the *Hubble Space Telescope* (550 km altitude) by *Brown et al.* [2003] and scaling to visible light yields brightnesses of a few $\times 10^{-17} B_\odot$ from orbiting platforms at that altitude. *DeForest and Howard* [2015] recently completed a digital feasibility study using single-blind degradation and restoration exercises with

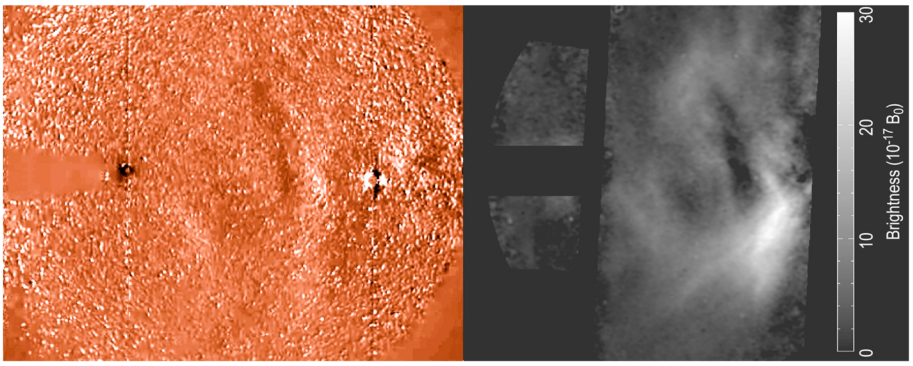

Figure 1. Recent improvements in the state of the art allow separation of a photometric signal from wide-field heliospheric images. (left) Median-filtered difference imaging was state of the art in 2010. (right) Processed image reveals shape and photometry in the same CME as at left.

STEREO/HI-2 data, and found that these backgrounds can be removed with slight variants of the techniques used for deep space.

High-Altitude Aurora. High-altitude aurora was discovered using SMEI [*Mizuno et al.*, 2005] and was a major contaminant in the SMEI signal (acquired from high LEO). Because the aurora is localized in space, it is also strongly time dependent when seen from an orbiting craft that flies under it. By collecting multiple images per orbit of each portion of the sky, one can identify and remove samples that are contaminated by aurora, preserving the remainder of the samples and thereby generating full field-of-view, aurora-free image data products by combining the multiple images from each orbit. This was not easily possible with SMEI because of limitations of its platform: SMEI was originally designed for a spinning platform but was later adapted to the three-axis stabilized, nadir-pointed Coriolis spacecraft [e.g., *Jackson et al.*, 2010]. Its linear detectors scanned around the sky as the spacecraft rotated, and SMEI therefore sampled each portion of the sky only once per orbit. A full 2-D imaging instrument, or a SMEI-like instrument on a spinning platform, would acquire multiple samples per orbit, enabling straightforward auroral background removal that was difficult to accomplish with SMEI.

Lunar Effects. Stray light from the Moon was a major issue for SMEI and was one reason why the SMEI team chose a small field of view that could be scanned across the sky. Generally, if the Moon enters the instrument field of view or the broader field of regard of the instrument's baffle, then additional stray light can swamp the data. The Moon is in the same hemisphere as the Sun for roughly 2 weeks per month, and during that time data from either the east or west portion of the sky may be degraded. This may not impact a demonstration or scientific mission but requires consideration for an operational one, depending on requirements and baffle design.

Single LEO instruments with a full conical baffle are not strongly affected by the Moon, provided that the field of view is fully steerable: a conventional vaned baffle that requires 20° clear field from the Sun to achieve $10^{-13}B_\odot$ rejection of stray sunlight may only require 10° from the full Moon to achieve the same level of stray moonlight rejection, due to the 10^{-6} reduction in intensity of the Moon compared to the Sun. Further, when the Moon is in the field of regard of an inner heliospheric imager, it has a high phase angle, further reducing the effect of moonlight.

A single LEO CubeSat with a simple truncated-plane corral style baffle (as described in section 5.1) is more subject to lunar interference, because it relies on having a full clear hemisphere to work. However, a smallsat or constellation (with a slightly larger baffle than is feasible with a CubeSat), in an appropriate Sun-synchronous polar orbit, could image over 340° of azimuth at all times, cutting out the 20° range surrounding the Moon during the times it crosses near the Sun.

2.4. Spatial Resolution for Prediction of SEPs and B_z

Increasing the spatial resolution of heliospheric imaging may enable new ways to predict space weather events: CME geoeffectiveness (via B_z proxy) and solar energetic particle (SEP) productivity (via shock turbulence measurement).

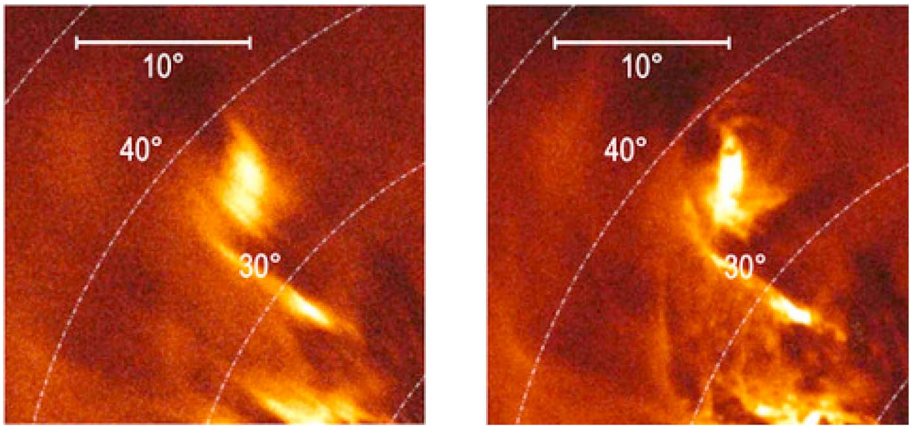

Figure 2. Spatial resolution limits current heliospheric imagers. (left) Simulated HI image based on an actual CME observed with LASCO, with imposed motion blur to account for the STEREO/HI-2 exposure time. (right) The same feature has negligible blur when exposure time is short, aiding tracking and possibly helping to predict B_z.

Heliospheric imaging does not require high spatial resolution compared with, say, telescopic solar remote sensing. The current generation of instruments are limited by noise and/or exposure characteristics rather than optical resolution. The effective spatial resolution of STEREO/HI-2 is governed by motion-blur effects, resulting in an effective resolution of 2° – 3°. That resolution is sufficient to track CME fronts and the largest scale substructures in the CMEs themselves. Higher spatial resolution would enable the characterization of shock fronts from both CMEs and CIRs, specifically the ability to detect ripples in shock structure that may produce elevated fields and, in turn, solar energetic particles [e.g., *Knock et al.*, 2003; *Giacalone and Jokipii*, 2007]. It is clear that foreseeable coronagraphs and heliospheric imagers cannot hope to resolve the leading edge structure of solar wind shocks — which exists on kinetic scales comparable to the proton gyroradius. However, extensive studies [e.g., *Vourlidas and Ontiveros*, 2009; *Vourlidas and Bemporad*, 2012; *Vourlidas et al.*, 2013; *Rouillard et al.*, 2014] have provided a large body of evidence that shocks can be located, characterized, and tracked using imaging of Thomson scattered light in the coronagraph field of view. By providing information on the density ahead of and behind the shock,and tracking the shock's propagation speed, such measurements yield all the important characteristics of a classic hydrodynamic shock, as well as determining the morphological evolution of the shock front. Extending this work to the outer corona and inner heliosphere is important for understanding the shock-SEP connection, and for predicting shock-associated SEP showers.

High spatial resolution imaging would also enable heliospheric tracking of the CME substructure that is visible in the coronagraphic field of view. In the corona, this substructure traces the magnetic structure of the CME [e.g., *Low and Berger*, 2003]. In principle, this could yield a new way to infer the sign of the north/south component of the magnetic field (B_z) in the leading portion of the CME. This B_z property is notoriously hard to predict because of the dual problems of determining B_z at the solar surface and understanding the effect of potential writhe as the CME departs from the Sun and propagates, despite recent promising work in this direction [*Jackson et al.*, 2015]. Additional complications arise because CMEs are optically thin, are extended 3-D structures, and change in kinematics and geometry in an asymmetric fashion. High spatial resolution heliospheric imaging may help with overcoming some of these problems, by allowing continuous tracking not only of the CME's overall bulk but also of the structure contained within it.

Recent work by *DeForest and Howard* [2015] shows that it is possible to operate deep space instruments comparable to STEREO/HI-2 with 10× shorter exposure time, with no significant degradation of photometry. This would reduce the motion blur by a factor of 10, yielding heliospheric images with scale-relative resolution comparable to that of coronal imagery from SOHO/LASCO. The effect is illustrated in Figure 2. Because motion-blur effects, and not optics, limit the resolution of current instruments, it may be possible to gain a 10× or better spatial resolution improvement simply by optimizing the exposure time of the instrument.

2.5. Dynamic Range and Noise

Photometric precision is the driving requirement for heliospheric imagers: relative photometric precision of reported radiances must be quite high to ensure adequate background subtraction even for qualitative geometric measurements. The starfield and *F* corona are the dominant sources of background light and

around the ecliptic plane and the Milky Way they are 100 times brighter than the desired Thomson scattering signal [e.g., *Jackson and Leinert*, 1985]. Flat-fielding, dynamic range, and stray light minimization drove the instrument and operational designs of both SMEI and the STEREO/HI instruments [*Eyles et al.*, 2003; *Jackson et al.*, 2010] and HI [*Eyles et al.*, 2009]. HI-2, in particular, creates very deep compound exposures: the nominal exposure time is 5000 s [*Eyles et al.*, 2009].

Because all heliospheric images must be background-subtracted to reveal the photometry of the solar wind features of interest [*DeForest et al.*, 2011], the noise characteristics of the final image are a combination of the usual camera noise sources (read noise, dark noise, and photon statistics), with residual errors in the background subtraction.

Heliospheric images are most appropriately calibrated in units of radiance, or surface brightness, of features in the field of view. In an image field, radiance (measured in either W m^{-2} sr^{-1} or, more commonly, in units of $B_\odot$) is an intrinsic value that is averaged across an entire feature, while *intensity* (measured in either W m^{-2} or multiples of the "solar constant" $I_\odot$) is an extrinsic value that must be summed/integrated over an entire feature. Each resolution element or pixel on the image plane reports the sum of a pixel-averaged radiance and a noise term. The noise terms are independent samples of a random variable, so averaging over larger regions of the image yields lower noise levels. To constrain the noise level, it is necessary to quote both the radiance noise floor and a spatial scale at which it is achieved.

DeForest and Howard [2015] analyzed the noise floor of HI-2 images processed with their pipeline and found that the limiting factor is not photon noise but rather errors in the a posteriori starfield model extracted from the data themselves. The principal errors in starfield model extraction arise from (1) residual pointing error-from frame-to-frame fits in the starfield evolution, (2) flat-field errors, and (3) uncorrected nonlinearity in the detector calibration, which causes photometric errors in calculated star intensities. Based on the statistical relationship between the noise and the brightness of the starfield, they concluded that the dominant error is due to uncorrected nonlinearity in the net response of the instrument. It is not clear whether this limiting factor is due to saturation in individual detector pixels [*Tappin et al.*, 2015] or to nonlinear response of the CCD detector (C. Eyles, private communication, 2011). The lesson to be taken is that detector characterization is critical to quantitative heliospheric imaging, and limits noise levels more strongly than does photon-counting Poisson noise in current instruments.

3. Polarization Properties of Thomson Scattered Light

The first coronagraph included a polarizer [*Lyot*, 1932], and spaceborne coronagraphs have provided polarized and unpolarized images since the days of Skylab [*MacQueen et al.*, 1974], potentially yielding 3-D locations of features observed in the corona [*Billings*, 1966]. Despite this extensive heritage, few papers have been published describing science that takes advantage of this capability. These limited works include important papers by *Poland and Munro* [1976], *Crifo et al.* [1983], *Moran et al.* [2010], *Mierla et al.* [2010], and *de Koning and Pizzo* [2011]. We can only speculate as to the reasons for this sparsity of work. It may be because of the lack of apparent need for such work in the early exploratory years, the level of complexity involved in extracting and analyzing features from polarized coronagraph data, or the familiar front/back ambiguity in the coronagraph field of view. The ambiguity, in particular, makes interpretation of the polarization signal difficult in the small-angle coronagraph field of view, even once noise and other instrumental considerations are accounted for.

Measurement of CME/CIR 3-D location is critical to precise prediction of space weather at Earth [*Webb et al.*, 2009]. It has been demonstrated that it is possible to extract 3-D information on CMEs from a single vantage point, using the polarization properties of Thomson scattering [*DeForest et al.*, 2013a; *Howard et al.*, 2013; *Xiong et al.*, 2013a, 2013b]. In this section we explore how this is accomplished and show how it could be utilized in a polarizing heliospheric imager.

3.1. Polarimetry in Thomson Scattered Visible Light: A Brief Review

The physics of Thomson scattering is well known and has been exploited in the context of solar physics since the earliest days of the coronagraph [*Lyot*, 1932; *Billings*, 1966; *Howard and Tappin*, 2009]. Figure 3 shows the geometry. Sunlight incident on a population of free electrons is divided into two linear polarizations: one in the plane of scatter and one perpendicular to it. The perpendicular component of the light is scattered without regard for scattering angle χ, while the in-plane component is projected as $\cos^2(\chi)$. At 90° scatter, the in-plane component is extinguished completely, the overall scattering is only 50% efficient, and the scattered

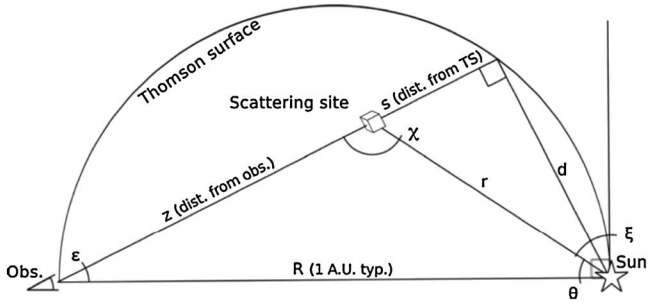

Figure 3. Heliospheric imaging geometry reveals the mechanism of polarization. The in-plane component of the electric field from incident sunlight is projected through the scattering angle χ. The "Thomson surface" is the locus where the scattering angle is 90°, as seen from a particular vantage point. It is the sphere whose diameter extends from the observer to the Sun.

light is 100% polarized in the direction tangential to the solar limb. The polarization properties therefore vary with varying χ in a predictable manner.

The point of closest approach to the Sun along the line of sight through the scattering electrons lies where $\chi = 90°$. Consequently, the inefficiency in the scattering function near 90° is balanced by the increase in the intensity of sunlight at this point of closest approach to the Sun. The two effects cancel nearly perfectly over a wide range of solar exit angles, leading to a "Thomson plateau" in which the total (unpolarized) radiance of a solar wind structure is independent of its exit angle from the Sun. The Thomson plateau effect mimics the form of uniform conventional reflective illumination [*Howard and DeForest*, 2012b], and makes heliospheric imagers about equally sensitive, aside from perspective effects, to structures exiting the Sun at all space-weather-relevant angles.

At all scattering angles, the tangential polarized brightness (or radiance) B_T from Thomson scattering in the solar wind is greater than or equal to the radial polarized brightness B_R. The sum of these two signals is the total brightness B, and the difference between them, pB, is always nonnegative due to the physics of Thomson scattering. Moreover, the ratio pB/B is determined by the scattering geometry and can be used to determine the position of each observed feature.

pB/B ratios have been used by a very few authors to locate structures observed with coronagraphs [e.g., *Mierla et al.*, 2010, and references therein; *de Koning and Pizzo*, 2011], but determinations in the corona are subject to a front/back ambiguity [e.g., *DeForest et al.*, 2013a]. The wider field of view provided by heliospheric imagers breaks the front/back ambiguity. This occurs because solar wind features propagate approximately radially. Of the two possible paths for a sequence of pB/B measurements of a feature in the heliosphere, one path is

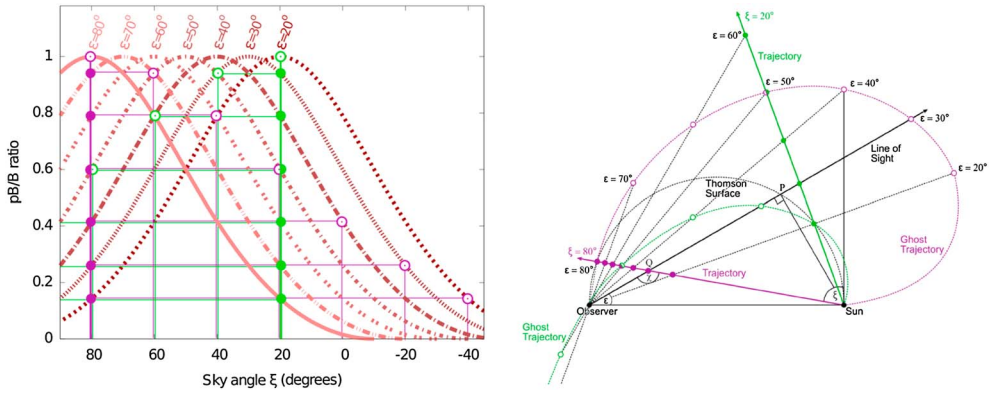

Figure 4. Polarization profiles of individual features at different locations reveal the exit angle of the feature relative to the Thomson surface (Figure 3). (left) Each curve shows the polarization fraction of a feature seen at a particular apparent distance (elongation) ε from the Sun versus the angle from the plane of the sky. (right) For a given polarization fraction, two trajectories are possible. One is correct, and the other is obviously nonphysical [*DeForest et al.*, 2013a]. This enables unambiguous location of space weather relevant disturbances in 3-D.

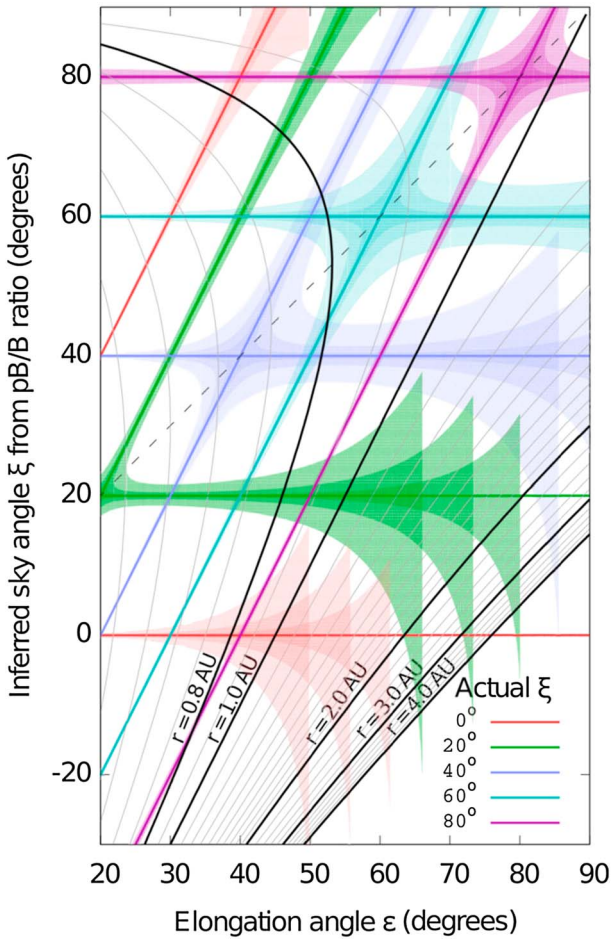

Figure 5. Inverting the curves in Figure 4 shows analytic feature location performance for five small test features. Features with high out-of-sky angle (ξ) are the most important for space weather prediction because they are approaching the observer. They are also the easiest to locate (smallest error bars). Nested curves are error bars at signal-to-noise ratios of 10, 30, and 100 on the R = 0.8 AU curve [*DeForest et al.*, 2013a].

approximately radial and the other is highly nonphysical (Figure 4). It is worth reiterating that this symmetry breaking is only achievable because heliospheric imagers observe across a large angular range in the sky.

3.2. Locating Small Features With Polarization

Small, dense features in the solar wind can be located in 3-D analytically via polarized imaging with moderate signal-to-noise ratio.

The applied theory of small-feature location has been developed at length by *DeForest et al.* [2013a]. Small features (whose length scale is negligible compared to the observer-feature distance) can be treated as points. The polarization characteristics of the feature are then straightforward to calculate by applying the basic theory of Thomson scattering. Figure 4 shows how the polarization characteristics of a small feature vary with its position relative to the observer (angles defined in Figure 3). The curves in Figure 4 may be inverted analytically. Figure 5 shows the expected precision of this method. Five small features (each given a colored curve) with various signal-to-noise ratios were launched radially at different sky angles ξ relative to the observer. The shape of the curve shows the resulting analytic determination of feature position entirely from the polarization of the feature. The actual positions (radial motion; constant ξ) are given in the plot legend. The nested curves show error bars for photometric signal-to-noise ratios of 10, 30, and 100 at a distance of 0.8 AU from the Sun. The associated signal-to-noise ratio degrades as each feature propagates from the Sun and grows fainter. The inversion in Figure 5 assumes self-similar expansion, which is pessimistic. Dense wind features typically remain compact in the radial direction and may even accrete mass as they propagate. Hence, even with the same relative noise level at 0.8 AU, the error bars surrounding real feature determinations will likely

be smaller. Even from a lateral vantage point such as L5, the *pB/B* ratio adds crucial information about whether an observed feature will impact Earth or not.

3.3. Locating Corotating Interaction Regions

One unexpected capability arising from heliospheric observations was their ability to identify corotating interaction regions (CIRs) with relative ease. Prior to the discovery of this capability, workers were only able to directly measure CIRs in situ as they impacted spacecraft capable of measuring their signatures [e.g., *Smith and Wolfe*, 1976; *Pizzo*, 1982; *Gosling and Pizzo*, 1999; *Choi et al.*, 2009]. This severely hampered our ability to predict their arrival at Earth, as the time between the arrival of the CIR at the in situ spacecraft and at Earth was small. It is now known that CIRs produce an easily recognized signature, particularly in STEREO A imaging data, as the location of the spacecraft to the west of the Sun-Earth line placed it in a favorable location to observe the developed CIR front far from the Sun, prior to its arrival at Earth [see, e.g., *Rouillard et al.*, 2008; *Tappin and Howard*, 2009a; *Wood et al.*, 2010]. These characteristic CIR signatures appear in a type of representation of SECCHI data known as a "J-map" [*Davies et al.*, 2009], where a lateral slice through an image data cube produces a map of brightness as a function of elongation and time [see *Rouillard et al.*, 2008, 2010; *Tappin and Howard*, 2009a; *Conlon et al.*, 2015 for some examples of J-maps of CIRs]. This has provided a new capability to predict CIR arrivals ahead of their arrival at 1 AU, as workers can observe the development of these signatures in the J-map hours, and potentially days, ahead of their arrival at 1 AU [e.g., *Davis et al.*, 2012].

Sadly, with the STEREO A spacecraft now on the east side of the Sun-Earth line and with STEREO B nonoperational (at the time of writing), it is rather difficult to use the existing heliospheric imagers for CIR impact prediction. Earth-interacting CIRs are much more difficult to observe from the east, due to the viewing geometry [*Sheeley et al.*, 2008; *Tappin and Howard*, 2009a; *Wood et al.*, 2010]. This problem could be overcome with the application of polarimetry. *DeForest et al.* [2013a] showed how the *pB/B* ratio changes with elongation angle, for a simulated "ideal" CIR (see their Figure 10). This was found to change considerably as the location of the CIR relative to the observer changes, in a manner that could be detected and modeled.

3.4. Locating CMEs With Polarization

CME tracking with near-optimally positioned, unpolarized heliospheric imagers (off the Sun-Earth line) has the potential to improve CME arrival time estimates compared to the current state of the art [*Webb*, 2013; *Webb et al.*, 2013; *Möstl and Aothers*, 2014], with predictions issued some 8–24 h before arrival. This is a surprisingly large residual error, considering that HI-2 yields an image of the CME every 2 h as it crosses the inner solar system. The error arises because CME tracking is difficult even with an optimally placed imager or stereoscopic pair of imagers [e.g., *Lugaz*, 2010]. In particular, (a) CME shape and structure couples to the inferred location of the CME [e.g., *Howard*, 2011]; (b) the CME interacts with the surrounding solar wind, accreting material as it propagates, which changes the shape of the leading edge [e.g., *Howard and DeForest*, 2012a] and further confounds stereoscopic or single-vantage inference of CME location; (c) CMEs and the surrounding solar wind are optically thin; (d) CMEs have large 3-D structure [see also *Howard*, 2015]; and (e) some CMEs may be deflected from their radial path [e.g., *Byrne et al.*, 2010].

Single-view polarization measurements assist in overcoming the problems of stereoscopy in two ways: (a) they contribute to the decoupling of the two problems of understanding the leading edge *shape* and *location*, which improves even crude envelope models as demonstrated by *T. A. Howard et al.* [2013]; and (b) they enable unambiguous identification of substructures within the CME between the two polarized channels (radial and tangential) because the images are acquired from the same location and can be fully coaligned. Stereoscopic location of small subfeatures within CMEs is confounded by the difficulty of reliably identifying a particular parcel of plasma from multiple viewpoints, but a *pB/B* image pair from the same instrument can be coaligned precisely, because the vantage point is identical. Even if the two polarized images use two different optical trains with different distortion/projection functions, cross-image alignment can be accomplished with the starfield and optimized resampling [*DeForest*, 2004; *DeForest et al.*, 2011]. The improvement of 3-D reconstruction techniques has been demonstrated by *de Koning and Pizzo* [2011], using coronagraph data. They were able to refine the 3-D reconstruction of CMEs from a sharp polygon to a "fuzzy blob" structure, thereby improving the prediction of their impact likelihood with the Earth.

Although CMEs require shape modeling to determine their location [e.g., *Vourlidas and Howard*, 2006; *de Koning et al.*, 2009; *Webb et al.*, 2009, 2013] using the envelope of the CME (as distinct from the potential to locate small substructures using high spatial resolution), even crude CME propagation models are improved

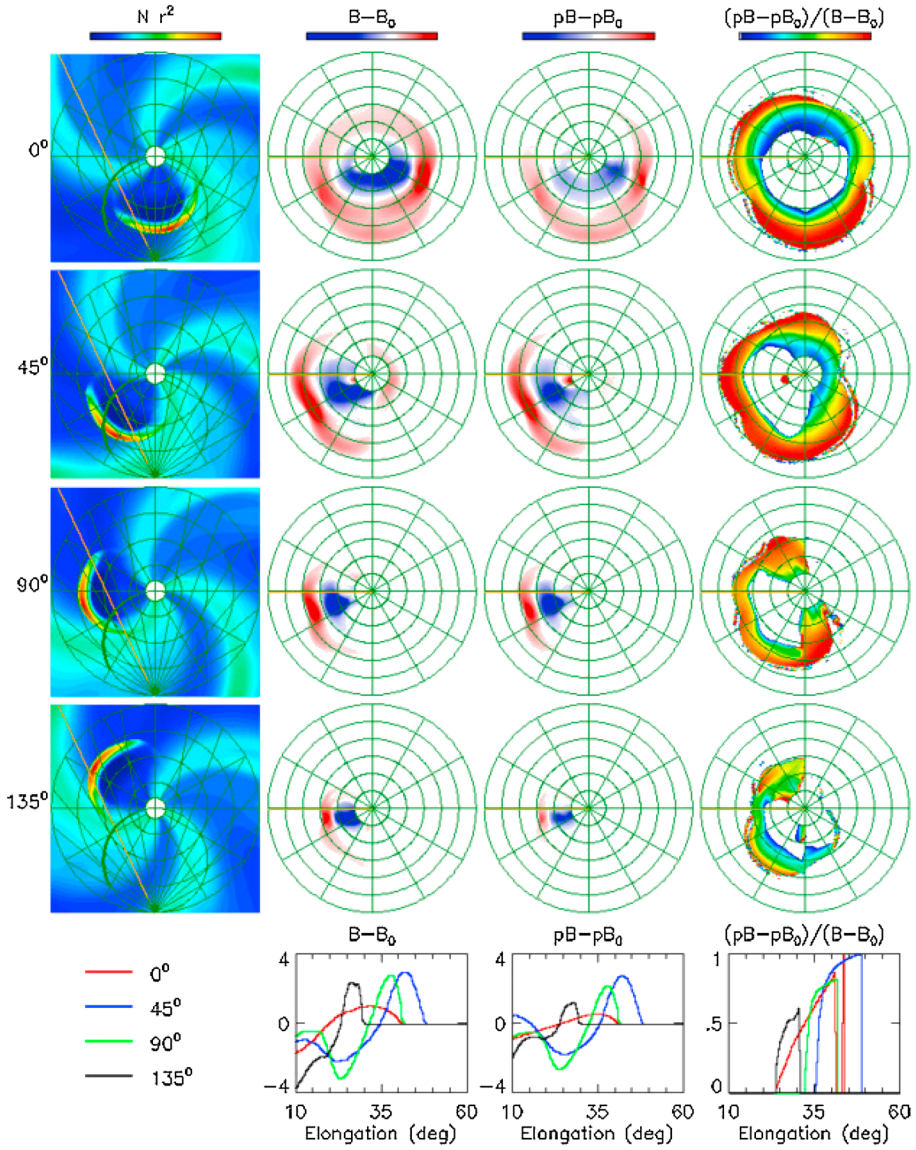

Figure 6. Polarimetric images of an ENLIL-modeled CME through a simulated polarizing imager show clear variation between unpolarized (*B*) and excess polarized (*pB*) brightness. Each row presents the same CME seen at a different out-of-lane angle. (first column) Top view of the simulated solar system with CME. (second to fourth columns) The CME's appearance in *B*, *pB*, and *pB/B*. (fifth row) Plots of each column's image parameter along the orange radial line on the left side of each image, for contrast/comparison.

by polarimetry. Recent work by *T. A. Howard et al.* [2013] showed how CME appearance changes in polarized imagery, depending on location in the solar system (Figure 6). They used the *pB/B* signal as a crude constraint on a simple model of CME propagation, where the CME was approximated as a simple expanding sphere. Their results compared favorably with those from a more sophisticated 3-D reconstruction tool (the TH model) [*Tappin and Howard*, 2009b], the latter unconstrained by polarization measurements, in the space weather relevant case of the CME propagating toward Earth. *T. A. Howard et al.* [2013] conclude that existing models can be improved significantly by the mere inclusion of *pB/B* heliospheric images as an additional constraint, although further improvement is achievable with more work. A similar analysis of a simulated interplanetary shock by *Xiong et al.* [2013a] led them to recommend that interplanetary polarization measurements would be of significant benefit in the study of CMEs. *Xiong et al.* [2013b] have also considered the benefit of white light polarization measurements, in combined heliospheric imaging and radio Faraday rotation studies, in determining CME magnetic field evolution.

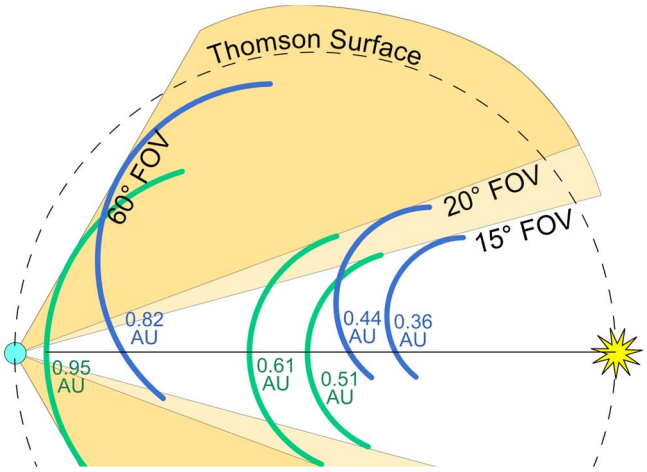

Figure 7. CMEs can be tracked over half of the Sun-Earth journey with a 15°–60° annular field of view. This view diagram shows a simple typical CME leading edge model in relation to a 15°–20° inner edge and 60° outer edge FOV for a model heliospheric imager near Earth. Green fronts show the path of a "direct hit" Earth-directed CME, and blue fronts show a "glancing blow" CME directed 30° to one side of Earth. The pictured locations are where the front crosses the inner or outer edge of the field of view. The marked distances are the distances of the front from the Sun along the Sun-Earth line in that geometry.

4. Mission Requirements for a Space Weather Operational Imager

The principal observing requirements for space weather imaging are spatial resolution, field of view, cadence, and photometric dynamic range. Here we define and discuss an approximate requirements envelope for an operational space weather heliospheric imager at either LEO, L1, or L5, whose primary purpose is to track CMEs and CIRs in 3-D as they propagate.

Spatial Resolution: 10 arcmin. Resolution requirements for space weather monitoring are set by the need to perform background subtraction of the starfield rather than the need to resolve the structure of the CME. The STEREO/HI-2A images, with 8–9 arcmin resolution (4 arcmin pixels) have adequately high resolution for our existing background-subtraction pipeline [*DeForest et al.*, 2011] to work, while STEREO/HI-2B with 40–60 arcmin optical resolution, does not. While background subtraction technology may improve, 8–10 arcmin resolution is the requirement with currently available postprocessing technology. The STEREO/HI-2 CME images are limited to 2°–3° spatial resolution by motion blur, and this is sufficient to track CME fronts and shapes—but does not drive the resolution requirement.

Field Of View: 15–20° to 60° Elongation; 160° Annular Coverage in Two 80° Extents Centered on the Ecliptic. Field of view requirements stem from the need to track CMEs close enough to the Sun to develop reasonable lead times and far enough from the Sun to establish their motion profile as they approach 1 AU. Note that this is independent of the FOV requirement for a coronagraph which would identify coronal and CME launch characteristics at smaller elongations. Using a simple "typical CME" leading-edge model with a circular leading edge whose minor radius is 1/3 of the distance from the leading edge to the Sun (Figure 7), it is possible to determine analytically the distances at which a CME is visible and trackable. As with coronagraphs, the natural field of view is an annulus centered on the Sun.

Inner/Outer Edges. Placing the inner edge at 15°–20° gives 9–12 h warning for a fast (1800 km/sec) CME traveling straight along the Sun-Earth line or more warning for oblique angles or slower speed. Placing the outer edge at 60° allows tracking the "leading edge" of the CME over all but the last 5%–20% of its journey for an imager at LEO or L1 (Figure 7).

Annular Extent. To observe all space-weather-relevant CMEs, a heliospheric imager needs to observe at least ± 40° above and below the ecliptic plane (total of 160° annulus in two 80° extents). More annular coverage is better, allowing better north/south centroiding of inbound CMEs. From a near-Earth vantage point, the eastern extent is the most important for CIRs, and the western extent is marginally more important for CMEs, because CIRs approach from the eastside and westernside CMEs tend to be slightly more productive of delayed SEPs.

Cadence: 2 h. This cadence requirement stems from the need for frequent samples of CME progress and for timely updates by forecasters on the ground. Further, for polarized 3-D heliospheric imaging multiple samples of each CME are needed to distinguish the front/back ambiguity of the Thomson scattering physics through evolution of the derived out-of-sky-plane angle. Two hour cadence is sufficient to achieve 4–12 samples over the required field of view for most direct hit Earth-directed CMEs; current techniques require four samples to establish trajectory [e.g., *Howard and Tappin*, 2010]. With 2 h cadence and the CME model described in Figure 7, it is possible to derive unambiguous (single-frame) trajectories with 10–12 h warning before impact in the fastest (>1800 km/sec) Earth-directed events and full 3-D (four frame) trajectories with 6–10 h warning for those same events—neglecting transfer and processing latency from the spacecraft. Assuming 1 h for transfer and one for processing, this yields 4 h warning for a full 3-D trajectory in the fastest Earth-directed event. Note that more warning time can be achieved with a combination of faster cadence, smaller elongation of the inner FOV edge, or lower transfer latency.

Photometric Dynamic Range: Noise $< 2\times10^{-16}B_{\odot}$*(1°× 1° Average).* The dynamic range requirement stems from the need to identify feature-excess photometry in both *B* and *pB* far from the Sun. The requirement is complicated by the scale-dependence of noise in a heliospheric imager. Measurements of the radiance of a feature involve *averaging* the brightness of the feature over its extent in the field of view and each pixel in the feature includes a separate sample of the noise field in the instrument. Large features include more pixels and their intensity, therefore, is summed across more samples of the noise. For this reason, photometry of large features is more precise than photometry of small features. Hence, it is necessary to quote both a radiance/brightness and a scale to specify the dynamic range. It is convenient to scale all dynamic range requirements to a 1° square patch of sky. The noise floor of a photometric measurement scales like the square root of the number of samples, i.e., linearly in the length scale of a square patch of image. Bright CMEs have typical intrinsic brightnesses of $2–5\times10^{-15}B_{\odot}$, 40° from the Sun [*Jackson et al.*, 2010; *DeForest et al.*, 2011]. To determine their structure at STEREO-like resolution and a signal-to-noise ratio of 30, the instrument must have a noise floor of $7\times10^{-17}B_{\odot}$ on a 3° × 3° patch of sky or $2\times10^{-16}B_{\odot}$ in each square degree of sky. This is the ultimate postprocessed noise floor, which is not limited by photon statistics in current instrumentation (see section 2.5).

5. Mission Concepts and Status

No polarized heliospheric imager has flown to date, despite the success of the unpolarized imagers Coriolis/SMEI and STEREO/HI and the development of the Solar Orbiter/SOLOHI [*R. A. Howard et al.*, 2013] and Solar Probe Plus/Wide-Field Imager for Solar Probe Plus [*Vourlidas et al.*, 2015] instruments. This is partly because, until improved background subtraction techniques were developed for STEREO/HI [*DeForest et al.*, 2011], it was not possible to carry out accurate photometry on CMEs more than a few degrees from the Sun. The benefits of polarizing heliospheric imagery all derive from being able to compare relative brightness of features in the heliosphere. We note that photometric analysis of feature-excess brightness in the heliosphere is a relatively new field.

Polarimetric heliospheric imaging has been thoroughly studied and is now ready for implementation in a scientific mission. Before it can be implemented as part of an operational space weather suite, it needs a flight demonstration either on a scientific mission or as an operational prototype. Quantitative heliospheric imaging is only feasible from space, because of the bright and variable background imposed by Earth's atmosphere.

We envision three independent ways to achieve an operational capability for 3-D CME tracking with polarized heliospheric imaging. The first, adding capability to the Deep Space Climate Observatory (DSCOVR) line of operational spacecraft, could be accomplished by adding a Space-weather Heliospheric Imaging Experiment for DSCOVR (SHIELD) instrument to the follow-on mission to DSCOVR itself. The second, the Cubesat Operational Network Space-weather Tracking Experiment in LEO (CONSTEL), is a constellation of CubeSats in LEO. Either solution, SHIELD or CONSTEL, would use existing and/or planned space assets and polarized imaging to improve space weather tracking and prediction at a small fraction of the cost of alternatives. A third alternative that is more expensive but also has a higher potential scientific and operational yield is the PHELIX concept (B. Lavraud et al., The Polarizing HELiospheric Imager eXperiment for INSTANT, submitted to *Journal of Atmospheric and Solar-Terrestrial Physics*, 2015) for mounting on a mission to L5.

5.1. Demonstration in LEO: CHIME and PHI-C

Demonstrating polarizing heliospheric imaging could be achieved by deploying a test-grade imager in LEO. Several such mission concepts have been developed by SwRI and other organizations including University

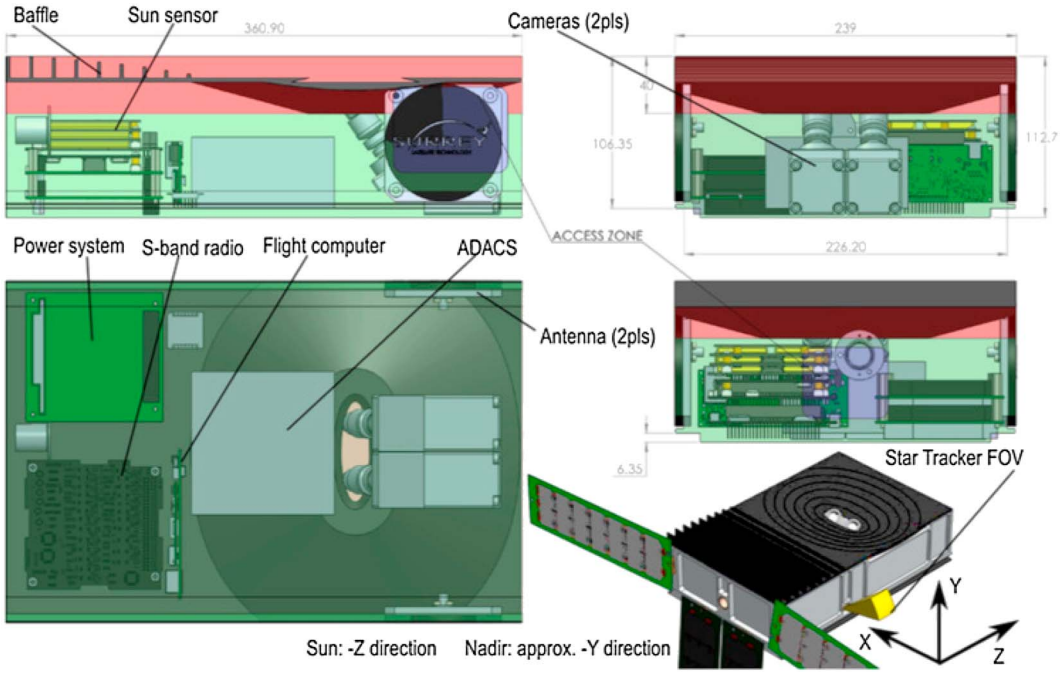

Figure 8. PHI-C is a SwRI-developed CubeSat concept that can demonstrate polarized heliospheric imaging in a 6U (36 cm × 22 cm × 11 cm) package. It uses a commercial off-the-shelf attitude system to steer the CubeSat to the correct observing geometry and relies on orbital geometry to hide the Earth below the baffle.

of California, San Diego, and Rutherford Appleton Laboratory Space. For example, the Cubesat Heliospheric Polarizing Heliospheric Imager CubeSat (CH-PHI) and Polarizing Heliospheric Imager CubeSat (PHI-C) mission concepts both use a single cubesat bus that deploys to LEO, with quasi-planar corral baffle that obscures the Earth and Sun. PHI-C, in particular, would have an instantaneous 30–40° circular field of view, with closest approach to the Sun at 18° elongation (corresponding to a distance of around 70 $R_{\odot}$). A concept design for PHI-C is shown in Figure 8.

Dual wide-field cameras near the rear of the CubeSat could collect images in each of the two polarization states of interest (radial and tangential). The two data streams are processed separately and merged to form *pB* (excess polarized brightness) and *B* (total brightness) images of the inner heliosphere.

The limited size of the CubeSat form factor has a cost in operational flexibility and in scientific application. In particular, because of its truncated planar corral baffle, PHI-C can image the heliosphere only when it is crossing over the day/night terminator. In Sun-synchronous twilight orbit, PHI-C builds up a full annular exposure of the inner heliosphere once per orbit. In lower inclination or nontwilight orbits, it images only the portion of the heliosphere that is in the instantaneous field of view during terminator crossings.

5.2. CONSTEL: An Operational Nanosat Constellation in LEO

Multiple PHI-C CubeSats or slightly larger variants could be flown in a Sun-synchronous "string of pearls" configuration, to form an operational constellation at low up-front cost, or for scientific observations with more capability than would be possible with a single CubeSat (PHI-C). The CONSTEL concept exploits the low cost of mass producing smallsats to achieve reliability through spacecraft-level redundancy. This approach has been applied successfully in the commercial sector (e.g., Planet Labs' network of Earth-observing CubeSats, http://www.planet.com). Multiple smallsats, similar to the PHI-C concept, could be launched to Sun-synchronous LEO; their data would be merged on the ground to produce a full 320°--360° azimuth image of the inner heliosphere (Figure 9). With a single PHI-C, cadence is limited to the 90–100 min period of LEO, but with a constellation of four to six buses, higher cadence and lower latency are possible.

The chief advantage of CONSTEL as an operational space weather mission is that it is inexpensive up-front and yields an incremental approach to an operational class asset: mass production reduces nonrecurring engineering (NRE) and project costs, while the CubeSat-like platform allows direct purchase of major subsystems from commercial off-the-shelf (COTS) providers for integration into each spacecraft. CONSTEL operations

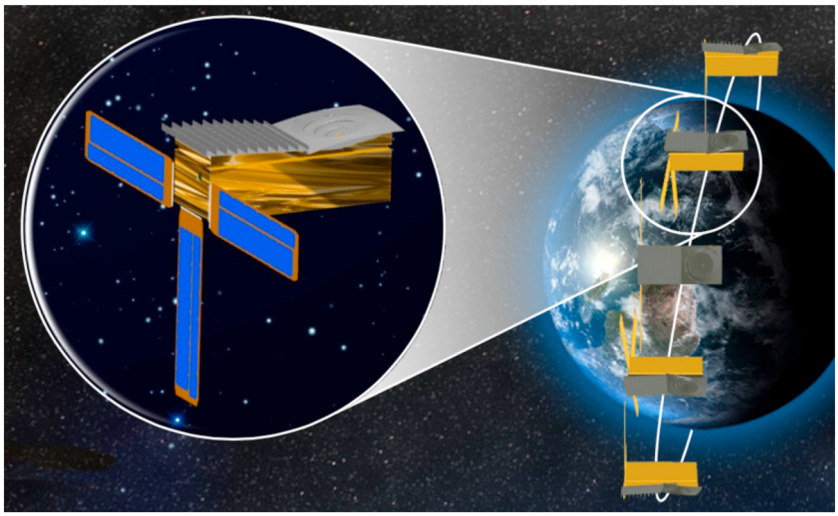

Figure 9. CONSTEL is a concept for an operational space weather heliospheric imaging system comprising three to five smallsats in space plus standby units on the ground.

require an ongoing development-and-launch program for new units as the smallsats wear out or reenter on a 2 year time frame rather than the 5–10 year design life of GOES-mounted assets. This requires ongoing funding to maintain the system with sufficient redundancy to achieve operational class reliability, although the anticipated 1-2 year design lifetime of each satellite would be well matched to a one-off scientific mission. The CONSTEL concept requires frequent ground contact from each bus to achieve low latency for space weather prediction. To keep data latency to under two orbital periods (200 min), a global network of ground stations is needed although, again, a scientific mission could accept longer latency and use fewer ground stations.

5.3. SHIELD: An Operational Instrument at L1 on DSCOVR Follow-On

SHIELD, a polarizing heliospheric imager at L1 on the DSCOVR follow-on (or similar spacecraft), would offer the benefits of deep-space imaging (no airglow, high-altitude aurora, or lunar incursion). SHIELD would yield operational improvements in prediction of CME and CIR arrival time and goeffectiveness, without the cost of a separate stand-alone mission.

The SHIELD concept is based on the instrument for the PHI-C demonstrator (Figure 8). It uses a miniature half-plane baffle and dual-camera system to minimize mass, though the baffle could be longer in SHIELD than in an actual CubeSat, improving dynamic range. Because DSCOVR does not rotate as would PHI-C or the CONSTEL spacecraft, operational coverage of the ecliptic plane would require two separate SHIELD instruments—East and West—mounted on opposite sides of DSCOVR. A rotating mission at L1 would not have this dual-instrument requirement. Full 360° azimuthal coverage from a three-axis stabilized platform would require a minimum of three instruments, with slightly different optical design from PHI-C.

The SHIELD concept exploits several lessons learned from the STEREO data: (1) dioptric systems (lenses) are preferred over radical catoptric (mirror) or catadioptric (lens-corrected mirror) systems, because lenses have superior polarization properties; (2) radically deep baffling is not required [*DeForest and Howard*, 2015], enabling a short, lightweight baffle; (3) instrument characterization and subsequent data processing are the dominant factors in heliospheric imaging system performance. These lessons, together, yield an affordable solution to heliospheric imaging with conventional optics and modest baffling. These results do not preclude radical reflective designs such as UCSD's Crystal Ball concept for unpolarized imaging [*Buffington et al.*, 1998] or SwRI's DAMASC concept (U.S. patent number 8,280,104) for wide-field unpolarized space weather tracking, but those designs may not be as suitable as a fully dioptric system for polarimetric heliospheric imaging because the wide-angle reflection would require more difficult compensation for instrumental polarization.

5.4. PHELIX: Heliospheric Imager Concept at L5

The Polarizing Heliospheric Imaging eXplorer (PHELIX), a polarizing heliospheric imager at L5 originally proposed for the INSTANT ESA class-S mission (B. Lavraud et al., submitted manuscript, 2015), would provide both direct perspective views at right angles to the Sun-Earth line for better tracking of CMEs and also 3-D location estimation of those CMEs to determine whether they will impact Earth (Figure 10).

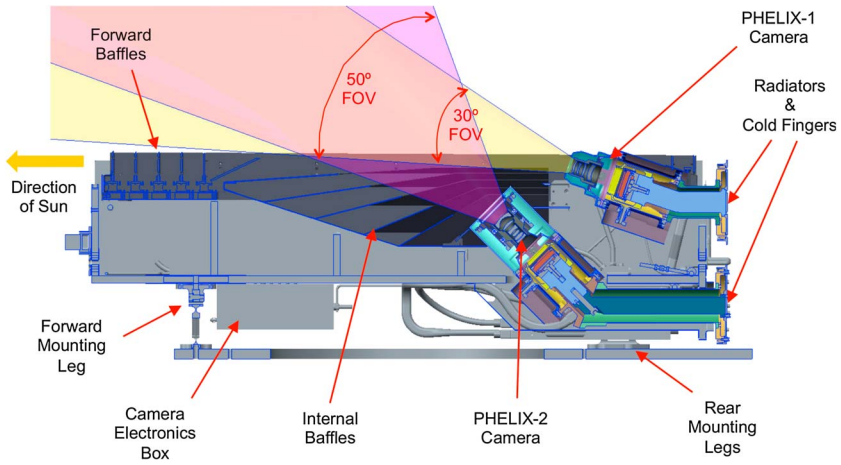

Figure 10. PHELIX is a concept for a scientific or prototype operational heliospheric imaging instrument to be flown at L5.

Like the above concepts, PHELIX is based on the STEREO HI design—but with even closer correspondence to the HI baffle and dual-camera layout than PHI-C, CONSTEL, or SHIELD. Because PHELIX would be flown to one side of the Sun-Earth line, breaking the symmetry of the observing geometry, it would only require one instrument to view in the general direction of the Sun-Earth line, rather than multiple cameras (as SHIELD) to view the full position angle annulus around the spacecraft.

A PHELIX instrument built for operational space weather prediction would, like the SHIELD concept, provide routine, regular imagery from deep space. Advantages include favorable viewing perspective, which increases utility for tracking even in the absence of polarized imagery; complete coverage via dual fields of view; and 3-D location of CMEs to better assess likelihood of Earth impact.

6. The Path Forward

Achieving an operational polarized heliospheric imaging capability requires a two-step approach. The NASA Technology Readiness Level (TRL) of unpolarized heliospheric imaging for predictive use is 8: it has been demonstrated in essentially operational-ready configuration, by the STEREO HI instrument. The TRL of *polarized* heliospheric imaging is 5: the technique has been validated in a relevant environment using forward modeling of simulated data: both for small scale features such as are seen in real solar wind images and for large scale, relatively smooth CME envelopes such as are commonly modeled for predictive purposes. Hence, a flight test or scientific demonstration mission is required before an operational system can be deployed, although the theory is well enough understood to support an exploratory scientific mission to LEO or deep space.

We have considered current status of the new technology of polarized heliospheric imaging for the specific application of space weather prediction. Further applications exist for scientific investigation of the heliosphere and solar wind but are not discussed in depth here. Polarized heliospheric imaging is a promising technology that should be developed for space weather prediction, and we have outlined several development paths for this exciting new technology.

Acknowledgments
The authors acknowledge insightful discussion and useful information from the following: the PHI-C, DELPHI, and PHELIX proposal teams; the L-5 Consortium; Doug Biesecker, Chris Eyles, Nat Gopalswamy, Bernie Jackson, James Tappin, and Angelos Vourlidas. The work also benefited from extensive and careful attention from the anonymous referees. This review was supported by internal research funds from Southwest Research Institute (DASH project) and from the NASA GI program (grant NNX13AE01G).

References

Bewsher, D., D. S. Brown, C. J. Eyles, B. J. Kellett, G. J. White, and B. Swinyard (2010), Determination of the photometric calibration and large-scale flat field of the STEREO heliospheric imagers: I. HI-1, *Sol. Phys.*, *264*, 433–460.

Bewsher, D., D. S. Brown, and C. J. Eyles (2012), Long-term evolution of the photometric calibration of the STEREO heliospheric imagers: I. HI-1, *Sol. Phys.*, *276*, 491–499.

Billings, D. E. (1966), *A Guide to the Solar Corona*, Academic Press, San Diego, Calif.

Broiles, T. W., M. I. Desai, C. O. Lee, and P. J. MacNeice (2013), Radial evolution of the three-dimensional structure in CIRs between Earth and Ulysses, *J. Geophys. Res. Space Physics*, *118*, 4776–4792, doi:10.1002/jgra.50482.

Brown, T. M., R. A. Kimble, H. C. Ferguson, J. P. Gardner, N. R. Collins, and R. S. Hill (2003), Measurements of the diffuse ultraviolet background and the terrestrial airglow with the space telescope imaging spectrograph, *Astron. J.*, *120*, 1153–1159.

Buffington, A (1998), Very-wide-angle optical systems suitable for spaceborne photometric measurements, *Appl. Opt.*, *37*, 4284–4293.

Buffington, A., P. P. Hick, B. V. Jackson, and C. M. Korendyke (1998), Corrals, hubcaps, and crystal balls: Some new designs for very-wide-angle visible-light heliospheric imagers, *Proc. SPIE*, *3442*, 77–86.

Byrne, J. P., S. A. Maloney, R. T. McAteer, R. James, J. M. Refojo, and P. T. Gallagher (2010), Propagation of an Earth-directed coronal mass ejection in three dimensions, *Nat. Commun.*, *1*, 74, doi:10.1038/ncomms1077.
Choi, Y., Y.-J. Moon, S. Choi, J.-H. Baek, S. Kim, K.-S. Cho, and G. S. Choe (2009), Statistical analysis of the relationships among coronal holes, corotating interaction regions, and geomagnetic storms, *Sol. Phys.*, *254*, 311–323.
Conlon, T. M., S. E. Milan, J. A. Davies, and A. O. Williams (2015), Corotating interaction regions as seen by the STEREO heliospheric imagers 2007-2010, *Sol. Phys.*, *290*, 2291–2309.
Crifo, F., J. P. Picat, and M. Cailloux (1983), Coronal transients—Loop or bubble?, *Sol. Phys.*, *83*, 143–152.
Davies, J. A., R. A. Harrison, A. P. Rouillard, N. R. Sheeley, C. H. Perry, D. Bewsher, C. J. Davis, C. J. Eyles, S. R. Crothers, and D. S. Brown (2009), A synoptic view of solar transient evolution in the inner heliosphere using the Heliospheric Imagers on STEREO, *Geophys. Res. Lett.*, *36*, L02102, doi:10.1029/2008GL036182.
Davis, C. J., J. A. Davies, M. Lockwood, A. P. Rouillard, C. J. Eyles, and R. A. Harrison (2009), Stereoscopic imaging of an Earth-impacting solar coronal mass ejection: A major milestone for the STEREO mission, *Geophys. Res. Lett.*, *36*, L08102, doi:10.1029/2009GL038021.
Davis, C. J., et al. (2011), A comparison of space weather analysis techniques used to predict the arrival of Earth-directed CME and its shockwave launched on 8 April 2010, *Space Weather*, *9*, S01005, doi:10.1029/2010SW000620.
Davis, C. J., J. A. Davies, M. J. Owens, and M. Lockwood (2012), Predicting the arrival of high-speed solar wind streams at Earth using the STEREO Heliospheric Imagers, *Space Weather*, *10*, S02003, doi:10.1029/2011SW000737.
DeForest, C. E. (2004), On re-sampling of solar images, *Sol. Phys.*, *219*, 3–23.
DeForest, C. E., and T. A. Howard (2015), Feasibility of heliospheric imaging from near Earth, *Astrophys J.*, *804*, 126.
DeForest, C. E., T. A. Howard, and S. J. Tappin (2011), Observations of detailed structure in the solar wind at 1 AU with STEREO/HI-2, *Astrophys. J.*, *738*, 103.
DeForest, C. E., T. A. Howard, and D. J. McComas (2012), Disconnecting open solar magnetic flux, *Astrophys. J.*, *745*, 36.
DeForest, C. E., T. A. Howard, and S. J. Tappin (2013a), The Thomson surface: II. Polarization, *Astrophys. J.*, *765*, 44.
DeForest, C. E., T. A. Howard, and D. J. McComas (2013b), Tracking coronal features from the low corona to Earth: A quantitative analysis of the 2008 December 12 coronal mass ejection, *Astrophys. J.*, *769*, 43.
de Koning, C. A., and V. J. Pizzo (2011), Polarimetric localization: A new tool for calculating the CME speed and direction of propagation in near-real time, *Space Weather*, *9*, S03001, doi:10.1029/2010SW000595.
de Koning, C. A., V. J. Pizzo, and D. A. Biesecker (2009), Geometric localization of CMEs in 3D space using STEREO beacon data: First results, *Sol. Phys.*, *256*, 167–181.
Eyles, C. J., G. M. Simnett, M. P. Cooke, B. V. Jackson, A. Buffington, P. P. Hick, N. P. Waltham, J. M. King, P. A. Anderson, and P. E. Holladay (2003), The Solar Mass Ejection Imager (SMEI), *So. Phys.*, *217*, 319–347.
Eyles, C. J., et al. (2009), The heliospheric imagers onboard the STEREO mission, *Sol Phys.*, *254*, 387–445.
Giacalone, J., and J. R. Jokipii (2007), Magnetic field amplification by shocks in turbulent fields, *Astrophys. J.*, *663*, L41.
Gosling, J. T., and V. J. Pizzo (1999), Formation and evolution of corotating interaction regions and their three dimensional structure, *Space Sci Rev.*, *89*, 21–52.
Harrison, R. A., et al. (2008), First imaging of coronal mass ejections in the heliosphere viewed from outside the Sun Earth line, *Sol. Phys.*, *247*, 171–193.
Harrison, R. A., et al. (2009), Two years of the STEREO Heliospheric Imagers, *Sol. Phys.*, *256*, 219–237.
Harrison, R. A., et al. (2012), An analysis of the origin and propagation of the multiple coronal mass ejections of 2010 August 1, *Astrophys. J.*, *750*, 45.
Howard, R. A., et al. (2008), Sun Earth Connection Coronal and Heliospheric Investigation (SECCHI), *Space Sci. Rev.*, *136*, 67–115.
Howard, R. A., et al. (2013), The solar orbiter imager (SoloHI) instrument for the Solar Orbiter mission. paper SPIE 8862 presented at Solar Physics and Space Weather Instrumentation V 88620H-1, San Diego, Calif., 25 Aug.
Howard, T. A. (2011), Three-dimensional reconstruction of coronal mass ejections using heliospheric imager data, *J. Atmos. Sol, Terr. Phys.*, *73*, 1242–1253.
Howard, T. A. (2015), Regarding the detectability and measurement of coronal mass ejections, *Space Weather Space Clim.*, *5*, A22.
Howard, T. A., and S. J. Tappin (2009), Interplanetary coronal mass ejections observed in the heliosphere: 1. Review of theory, *Space Sci. Rev.*, *147*, 31–54.
Howard, T. A., and S. J. Tappin (2010), Application of a new phenomenological coronal mass ejection model to space weather forecasting, *Space Weather*, *8*, S07004, doi:10.1029/2009SW000531.
Howard, T. A., and C. E. DeForest (2012a), Inner heliospheric flux rope evolution via imaging of coronal mass ejections, *Astrophys. J.*, *746*, 64.
Howard, T. A., and C. E. DeForest (2012b), The Thomson surface: I. Reality and myth, *Astrophys. J.*, *752*, 130.
Howard, T. A., and C. E. DeForest (2014), The formation and launch of a coronal mass ejection flux rope: A narrative based on observations, *Astrophys. J.*, *796*, 33.
Howard, T. A., and C. E. DeForest (2015), Observations of a solar wind domain boundary extending 1 AU from the Sun, *Astrophys. J. Lett.*, *800*, L25.
Howard, T. A., C. E. DeForest, and A. A. Reinard (2012), White-light observations of solar wind transients and comparison with auxiliary data sets, *Astrophys. J.*, *754*, 102.
Howard, T. A., S. J. Tappin, D. Odstrcil, and C. E. DeForest (2013), The Thomson surface: III. Tracking features in 3D, *Astrophys. J.*, *765*, 45.
Jackson, B. V., and C. Leinert (1985), Helios images of solar mass ejections, *J. Geophys. Res.*, *90*, 10,759–10,764.
Jackson, B. V., A. Buffington, P. P. Hick, X. Wang, and D. Webb (2006), Preliminary three-dimensional analysis of the heliospheric response to the 28 October 2003 CME using SMEI white-light observations, *J. Geophys. Res.*, *111*, A04S91, doi:10.1029/2004JA010942.
Jackson, B. V., M. M. Bisi, P. P. Hick, A. Buffington, J. M. Clover, and W. Sun (2008), Solar Mass Ejection Imager 3-D reconstruction of the 27-28 May 2003 coronal mass ejection sequence, *J. Geophys. Res.*, *113*, A00A15, doi:10.1029/2008JA013224.
Jackson, B. V., A. Buffington, P. P. Hick, M. M. Bisi, and J. M. Clover (2010), A heliospheric imager for deep space: Lessons learned from Helios, SMEI, and STEREO, *Sol. Phys.*, *265*, 257–275.
Jackson, B. V., J. M. Clover, P. P Hick, A. Buffington, M. M. Bisi, and M. Tokumaru (2013), Inclusion of real-time in-situ measurements into the UCSD time-dependent tomography and its use as a forecast algorithm, *Sol. Phys.*, *285*, 151–165.
Jackson, B. V., P. P. Hick, A. Buffington, H.-S. Yu, M. M. Bisi, M. Tokumaru, and X. Zhao (2015), A determination of the north-south Heliospheric magnetic field component from inner corona closed-loop propagation, *Astrophys. J.*, *803*, 1.
Knock, S. A., I. H. Cairns, and P. A. Robinson (2003), Type II radio emission predictions: Multiple shock ripples and dynamic spectra, *J. Geophys. Res.*, *108*(A10), 1361, doi:10.1029/2003JA009960.
Lee, C. O., C. N. Arge, D. Odstrcil, G. Millward, V. J. Pizzo, and N. Lugaz (2013), Ensemble modeling of CME propagation, *Sol. Phys.*, *285*, 349–368.

Low, B. C., and M. A. Berger (2003), A morphological study of helical coronal magnetic structures, *Astrophys. J.*, *589*, 644.
Lugaz, N. (2010), Accuracy and limitations of fitting and stereoscopic methods to determine the direction of coronal mass ejections from heliospheric imagers observations, *Sol. Phys.*, *267*, 411–429.
Lyot, B. (1932), Étude de la couronne solarie en dehors des éclipses, *Z. Astrophys.*, *5*, 73.
MacQueen, R. M., J. T. Gosling, E. Hildner, R. H. Munro, A. I. Poland, and C. L. Ross (1974), The High Altitude Observatory white light coronagraph experiment, in *Proc. IAU Symp 57, Surfers Paradise, Australia, 7–11 Sept.*, edited by G. A. Newkirk, p. 505, D. Reidel, Boston.
Mierla, M., et al. (2010), On the 3-D reconstruction of coronal mass ejections using coronagraph data, *Ann. Geophys.*, *28*, 203–215.
Mizuno, D. R., et al. (2005), Very high altitude aurora observations with the Solar Mass Ejection Imager, *J. Geophys. Res.*, *110*, A07230, doi:10.1029/2004JA010689.
Moran, T. G., J. M. Davila, and W. T. Thompson (2010), Three-dimensional polarimetric coronal mass ejection localization tested through triangulation, *Astrophys. J.*, *712*, 453.
Möstl, C., and Aothers (2014), Connecting speeds, directions and arrival times of 22 coronal mass ejections from the Sun to 1 AU, *Astrophys. J.*, *787*, 119.
Möstl, C., M. Temmer, T. Rollett, C. J. Farrugia, Y. Liu, A. M. Veronig, M. Leitner, A. B. Galvin, and H. K. Biernat (2010), STEREO and Wind observations of a fast ICME flank triggering a prolonged geomagentic storm on 5–7 April 2010, *Geophys. Res. Lett.*, *37*, L24103, doi:10.1029/2010GL045175.
Odstrcil, D., and V. J. Pizzo (1999), Three-dimensional propagation of CMEs in a structured solar wind flow: 1. CME launched within the streamer belt, *J. Geophys. Res.*, *104*, 483–492.
Odstrcil, D., V. J. Pizzo, and C. N. Arge (2005), Propagation of the 12 May 1997 interplanetary coronal mass ejection in evolving solar wind structures, *J. Geophys. Res.*, *110*, A02106, doi:10.1029/2004JA010745.
Pizzo, V. J. (1982), A three-dimensional model of corotating streams in the solar wind: 3. Magnetohydrodynamic streams, *J. Geophys. Res.*, *87*, 4374–4394.
Poland, A. I., and R. H. Munro (1976), Interpretation of broad-band polarimetry of solar coronal transients—Importance of H-alpha emission, *Astrophys. J.*, *209*, 927.
Rollett, T., et al. (2014), Combined multipoint remote and in situ observations of the asymmetric evolution of a fast solar coronal mass ejection, *Astrophys. J.*, *790*, L6.
Rouillard, A. P., et al. (2008), First imaging of corotating interaction regions using the STEREO spacecraft, *Geophys. Res. Lett.*, *35*, L10110, doi:10.1029/2008GL033767.
Rouillard, A. P., et al. (2010), Intermittent release of transients in the slow solar wind: 1. Remote sensing observations, *J. Geophys. Res.*, *115*, A04103, doi:10.1029/2009JA014471.
Rouillard, A. P., et al. (2011), Interpreting the properties of solar energetic particle events by using combined imaging and modeling of interplanetary shocks, *Astrophys. J.*, *735*, 7.
Rouillard, A. P., A. Vourlidas, A. J. Tylka, C. K. Ng, and C. M. Cohen (2014), Coronal shocks properties and their associations with energetic particle events measured near 1 AU, Abstract SH43A-4170 presented at 2014 Fall Meeting, AGU, San Francisco, Calif., 15–19 Dec.
Sheeley, N. R. et al. (2008), SECCHI Observations of the Sun's garden-hose density spiral, *Astrophys. J.*, *674*, L109.
Sheeley, N. R., Jr., and A. P. Rouillard (2010), Tracking streamer blobs into the heliosphere, *Astrophys. J.*, *715*, 300.
Smith, E. J., and J. H. Wolfe (1976), Observations of interaction regions and corotating shocks between one and five AU—Pioneers 10 and 11, *Geophys. Res. Lett.*, *3*, 137–140.
Sparrow, J. G., J. L. Weinberg, and R. C. Hahn (1977), Ten-color Gegenschein-zodiacal light polarimeter, *J. Appl. Opt.*, *16*, 978–982.
Taktakishvili, A., M. Kuznetsova, P. MacNeice, M. Hesse, L. Rastätter, A. Pulkkinen, A. Chulaki, and D. Odstrcil (2009), Validation of the coronal mass ejection prediction at the Earth orbit estimated by ENLIL heliosphere cone model, *Space Weather*, *7*, S03004, doi:10.1029/2008SW000448.
Tappin, S. J., and T. A. Howard (2009a), Direct observation of a corotating interaction region by three spacecraft, *Astrophys. J.*, *702*, 862.
Tappin, S. J., and T. A. Howard (2009b), Interplanetary coronal mass ejections observed in the heliosphere: 2. Model and data comparison, *Space Sci. Rev.*, *147*, 55–87.
Tappin, S. J., C. J. Eyles, and J. A. Davies (2015), Determination of the photometric calibration and large-scale flatfield of the STEREO heliospheric imagers: II. HI-2, *Sol. Phys.*, *290*, 2143–2170.
Tokumaru, M. (2013), Three-dimensional exploration of the solar wind using observations of interplanetary scintillation, *Proc. Jpn. Acad., Ser. B*, *89*, 67–79.
Vourlidas, A., and A. Bemporad (2012), A decade of coronagraphic and spectroscopic studies of CME-driven shocks, *AIP Conf. Proc.*, *1436*, 279.
Vourlidas, A., and R. A. Howard (2006), The proper treatment of coronal mass ejection brightness: A new methodology and implications for observations, *Astrophys. J.*, *642*, 1216.
Vourlidas, A., and V. Ontiveros (2009), A review of coronagraphic observations of shocks driven by coronal mass ejections, *AIP Conf. Proc.*, *1183*, 139.
Vourlidas, A., B. J. Lynch, R. A. Howard, and Y. Li (2013), How many CMEs have flux ropes? Deciphering the signatures of shocks, flux ropes, and prominences in coronagraph observations of CMEs, *Sol. Phys.*, *284*, 179–201.
Vourlidas, A., et al. (2015), The Wide-Field Imager for Solar Probe Plus (WISPR), *Space Sci. Rev.*, doi:10.1007/s11214-014-0114-y.
Webb, D. F. (2013), Coronal mass ejections and space weather, in *Proc. IISTP, ASI Conf. Ser.*, vol. 10, edited by N. Gopalswamy et al., pp. 37.
Webb, D. F., T. A. Howard, C. D. Fry, T. A. Kuchar, D. R. Mizuno, J. C. Johnston, and B. V. Jackson (2009), Studying geoeffective interplanetary coronal mass ejections between the Sun and Earth: Space weather implications of Solar Mass Ejection Imager observations, *Space Weather*, *7*, S05002, doi:10.1029/2008SW000409.
Webb, D. F., et al. (2013), Heliospheric imaging of 3D density structures during the multiple coronal mass ejections of late July to early August 2010, *Sol. Phys.*, *285*, 317–348.
Weinberg, J. L., R. C. Hahn, and J. G. Sparrow (1975), The Skylab ten color photoelectric polarimeter, *Sci. Instrum.*, *1*, 407.
Wood, B. E., and R. A. Howard (2009), An empirical reconstruction of the 2008 April 26 coronal mass ejection, *Astrophys. J.*, *702*, 901.
Wood, B. E., R. A. Howard, A. Thernisien, and D. G. Socker (2010), The three-dimensional morphology of a corotating interaction region in the inner heliosphere, *Astrophys. J.*, *708*, 89.
Wood, B. E., C.-C. Wu, R. A. Howard, D. G. Socker, and A. P. Rouillard (2011), Empirical reconstruction and numerical modeling of the first geoeffective coronal mass ejection of Solar Cycle 24, *Astrophys. J.*, *729*, 70.

Wood, B. E., C.-C. Wu, A. P. Rouillard, R. A. Howard, and D. G. Socker (2012), A coronal hole's effects on coronal mass ejection shock morphology in the inner heliosphere, *Astrophys. J.*, *755*, 43.

Xiong, M., J. A. Davies, M. M. Bisi, M. J. Owens, R. A. Fallows, and G. D. Dorrian (2013a), Effects of Thomson-scattering geometry on white-light imaging of an interplanetary shock: Synthetic observations from forward magnetohydrodynamic modelling, *Sol. Phys.*, *285*, 369–389.

Xiong, M., J. A. Davies, X. Feng, M. J. Owens, R. A. Harrison, C. J. Davis, and Y. D. Liu (2013b), Using coordinated observations in polarized white light and Faraday rotation to probe the spatial position and magnetic field of an interplanetary sheath, *Astrophys. J.*, *777*, 32.